Journal of Zhejiang University-SCIENCE A (Applied Physics & Engineering)
ISSN 1673-565X (Print); ISSN 1862-1775 (Online)
www.jzus.zju.edu.cn; www.springerlink.com
E-mail: jzus@zju.edu.cn

Numerical research on the anti-sloshing effect of a ring baffle in an independent type C LNG tank*

Ge LIU[1], Yan LIN[†‡1,2], Guan GUAN[1], Yan-yun YU[1]

[1]*School of Naval Architecture, Dalian University of Technology, Dalian 116024, China*

[2]*State Key Laboratory of Structural Analysis for Industrial Equipment, Dalian University of Technology, Dalian 116024, China*

[†]E-mail: linyanly@dlut.edu.cn

Received May 18, 2017; Revision accepted Dec. 7, 2017; Crosschecked Aug. 16, 2018

Abstract: Liquid sloshing can be suppressed by the installation of baffles. The influence of a ring baffle on sloshing reduction is investigated based on an analysis of parameter sensitivity through computational fluid dynamics (CFD) simulation. Firstly, a series of liquid sloshing experiments with a liquefied natural gas (LNG) independent type C model tank is designed to validate the numerical method. Four definition parameters of the ring baffle, the height (H), the position installation (P), the inclined angle (θ), and the thickness (t), are selected as effective factors, and the efficiency of sloshing reduction is used as the comparison criterion. Research cases of parameter sensitivity are designed by orthogonal tests and computed by a validated numerical method. It is found that the thickness has little effect but the other parameters, especially the height, have significant influence in suppressing sloshing. The directions of improvement of the significant actors are analyzed. The effective height of the ring baffle is discussed numerically with different excitation angles. It is demonstrated that increasing the height of the ring baffle will not bring further improvement in efficiency of sloshing reduction after it exceeds 20% of the tank diameter.

Key words: Sloshing; Ring baffle; Independent type C liquefied natural gas (LNG) tank; Parameter sensitivity
https://doi.org/10.1631/jzus.A1700268 **CLC number:** U661.7

1 Introduction

The sloshing phenomenon is usually encountered in partially filled moving tanks, such as floating production storage and offloading (FPSO), floating storage and regasification unit (FSRU), liquefied natural gas (LNG) fuel bunker vessels in operation, and liquid storage tanks in dual engine ships or oil tank cars. This highly nonlinear phenomenon (Lu et al., 2016) may lead to violent impact pressures near the liquid free surface. When the lowest natural frequency of the liquid is close to the excitation frequency, sloshing becomes violent and significantly compromises structural safety and the stability of the vessel. Usually, installing sloshing suppressing devices is a practical and effective way of bringing energy dissipation and shifting the natural period of baffle-free sloshing (Cho and Kim, 2016).

Extensive investigations have been performed on devices for suppressing sloshing. Nonlinear liquid sloshing inside a partially filled rectangular tank has been investigated numerically by Celebi and Akyildiz (2002). They found that producing a shear layer, where energy is dissipated by viscous action, is a method of reducing sloshing by incorporating a baffle. The motion of the free surface induced by sloshing has a high speed. Therefore, Yu et al. (2017)

‡ Corresponding author

* Project supported by the National Research Program for High Technology Ship Development of China (No. MIIT 2014-498), the Science and Technology Project of Guangdong Province, China (Nos. 2015B090904010 and 2016B090918092), the Marine Renewable Energy Special Fund of China (No. QDME2013ZB01), the National Natural Science Foundation of China (No. 51609036), the Fundamental Research Funds for the Central Universities of China (No. DUT16RC(4)26), and the Doctoral Scientific Research Foundation of Liaoning Province, China (No. 201501176)

ORCID: Ge LIU, https://orcid.org/0000-0003-4140-1081

designed a floating baffle to block the oscillation of the free surface regardless of the filling ratio. The performance of the floating baffle is discussed experimentally and its dissipative mechanisms are obtained by numerical methods verified by experiments. Lloyd et al. (2002) studied experimentally several kinds of baffles, including solid dashed, oblique, spiral, round, and perforated ones. The experiments were conducted in a one-sixth scale model of a cryogenic road tank. Analogously, two types of baffles are discussed by Panigrahy et al. (2009) through a series of experiments. It can be found that, as a ring baffle can absorb the energy at the walls and dissipate it to all the walls, it is more effective than the conventional horizontal baffles. Wei et al. (2015) identified the solidity ratio of a slat-screen that provided an optimal suppressing function on wave elevation and slamming pressures on the vertical tank wall. Meanwhile, the authors found seven kinds of wave scenarios under the specified conditions. Cho and Kim (2016) theoretically and experimentally investigated the effect of a dual vertical slat-screen on sloshing reduction inside a rectangular tank. It was found that optimal porosity, submergence depth, and installation position play key roles in suppressing sloshing motions. Concentrating on the influence of a perforated vertical baffle, Xue et al. (2013) designed physical experiments to compare its effectiveness in reducing liquid sloshing. The suitable orifice size of a perforated baffle is considered for an effective baffle arrangement in tanks by weakening the sloshing amplitude at higher excitation frequencies. Other researchers have considered non-rectangular tanks. The damping characteristic of ring baffles in a vertical cylindrical tank was studied experimentally and numerically by Akyıldız et al. (2013). It has been concluded that the arrangement of ring baffles is an important factor in reducing sloshing loads. Kang and Liu (2010) also stated that the vertical position of the baffle in an oil tank is the key to reducing the force and rolling moment during turning and braking. That conclusion is validated by the computational fluid dynamics (CFD) method. Zhang et al. (2016) carried out their research on nickel ore slurry sloshing in a prismatic cargo hold. The critical height of the longitudinal baffle, which can maximize damping factor, was presented and discussed by a numerical method based on data from the experiments.

In general, baffles are the most widely used of sloshing suppressing devices because of their simplicity of installation and high performance (Kim and Lee, 2008). In this paper, the anti-sloshing efficiency of a ring baffle set in the LNG independent type C tank is investigated based on analysis of parameter sensitivity through a CFD simulation. The physical experiments are designed to validate the numerical method, which is used to access the damping effect of the ring baffle. To reduce the number of numerical tests, an orthogonal test design is applied in analysis of parameter sensitivity and the main influencing factor is determined. After that, this factor is numerically discussed to determine its critical level.

2 Numerical method and mathematical model

The excitation motion of the tank is longitudinal, namely, around the z axis and the origin of axis (Fig. 1). For efficiency of calculation, a half tank model simplified from the test model is used for the numerical calculation.

The viscous fluid sloshing in the tank is subject to a continuity equation and the Navier-Strokes equation. The governing equations are as follows.

(a) The continuity equation is

$$\frac{\partial \rho}{\partial t}+\frac{\partial \rho u_i}{\partial x_i}=0, \tag{1}$$

where ρ and u_i are density and velocity, respectively. t is the time.

(b) The Reynolds-averaged Navier-Stokes (RANS) equation is

$$\begin{aligned}&\frac{\partial}{\partial t}(\rho u_i)+\frac{\partial}{\partial x_j}(\rho u_i u_j)\\&=-\frac{\partial p}{\partial x_j}+\frac{\partial}{\partial x_j}\left[\mu\left(\frac{\partial u_i}{\partial x_j}+\frac{\partial u_j}{\partial x_i}-\frac{2}{3}\delta_{ij}\frac{\partial u_l}{\partial x_l}\right)\right]\\&\quad+\frac{\partial}{\partial x_j}\left(-\rho\overline{u_i'u_j'}\right),\end{aligned} \tag{2}$$

where p is the time averaged pressure; μ is the dynamic viscosity of water; δ_{ij} is the Kronecker delta;

$-\rho\overline{u}_i'\overline{u}_j'$ is the Reynolds stress term; subscripts i, j, and l are the coordinate directions.

In order to attain more reliability, especially in the case of LNG sloshing simulations, Wemmenhove et al. (2005) suggested that the compressibility of the air should be taken into account. As the compressibility of air has a great influence on the rising time of impact pressure when the fluid has a low viscosity (as water or LNG), the air in this study is treated as an ideal gas. Thus, the conservation of energy is also contained in the governing equations:

$$\begin{aligned}&\frac{\partial}{\partial t}\rho\left(e+\frac{u_i^2}{2}\right)+\nabla\cdot\rho u_i\left(e+\frac{u_i^2}{2}\right)\\&\quad=\nabla\cdot\left(k_{\text{eff}}\nabla T\right)+\nabla\cdot\left(\mu\cdot u_i\right)+\rho f_i u_i+S_{\text{E}},\end{aligned}\tag{3}$$

where e is the internal energy, k_{eff} is the effective thermal conductivity, ∇T is the temperature gradient, f_i is the body force vector, and S_{E} is the source term. However, as the variation of temperature during sloshing can be considered as small, the temperature in the fluid domain is regarded as constant.

The sloshing will be nonlinear and random, especially during resonance. Considering computational expense, a realizable k-ε turbulence model is adopted. The turbulent kinetic energy k and its rate of dissipation ε are obtained by

$$\begin{aligned}&\frac{\partial}{\partial t}(\rho k)+\frac{\partial}{\partial x_j}(\rho k u_j)\\&\quad=\frac{\partial}{\partial x_j}\left[\left(\mu+\frac{\mu_{\text{t}}}{\sigma_k}\right)\frac{\partial k}{\partial x_j}\right]+f_{\text{c}}G_k\\&\qquad+G_{\text{b}}-\rho(\varepsilon-\varepsilon_0)-\gamma_{\text{M}}+S_k,\end{aligned}\tag{4}$$

$$\begin{aligned}&\frac{\partial}{\partial t}(\rho\varepsilon)+\frac{\partial}{\partial x_j}(\rho\varepsilon u_j)\\&\quad=\frac{\partial}{\partial x_j}\left[\left(\mu+\frac{\mu_{\text{t}}}{\sigma_\varepsilon}\right)\frac{\partial\varepsilon}{\partial x_j}\right]+f_{\text{c}}C_{\varepsilon1}S\varepsilon+\frac{\varepsilon}{k}\left(C_{\varepsilon1}C_{\varepsilon3}G_{\text{b}}\right)\\&\qquad-\frac{\varepsilon}{k+\sqrt{\nu\varepsilon}}C_{\varepsilon2}\rho(\varepsilon-\varepsilon_0)+S_\varepsilon,\end{aligned}\tag{5}$$

where μ_{t} is the eddy viscosity coefficient; G_k is the turbulent production term; f_{c} is the curvature correction factor; G_{b} is the buoyancy production term; ε_0 is the ambient turbulence value in the source terms that counteracts turbulence decay; γ_{M} is the compressibility modification term; S_k and S_ε are user-specified source terms. $C_{\varepsilon1}$, $C_{\varepsilon2}$, and $C_{\varepsilon3}$ are the constant coefficients. σ_k and σ_ε are the turbulent Prandtl numbers for k and ε, respectively. S is the modulus of the mean strain rate tensor. v is the kinematic viscosity.

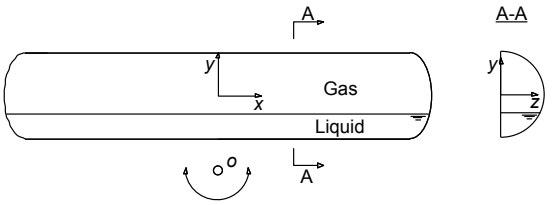

Fig. 1 Model for numerical computation

Unlike the standard k-ε turbulence model, in the realizable model the coefficient C_μ for attaining turbulent viscosity is computed as

$$C_\mu=\frac{1}{A_0+A_{\text{S}}\dfrac{kU^*}{\varepsilon}},\tag{6}$$

where

$$U^*=\sqrt{\boldsymbol{S}:\boldsymbol{S}+\boldsymbol{W}:\boldsymbol{W}},\tag{7}$$

$$\boldsymbol{S}=(\nabla\boldsymbol{u}+\nabla\boldsymbol{u}^{\text{T}})/2,\tag{8}$$

$$\boldsymbol{W}=(\nabla\boldsymbol{u}-\nabla\boldsymbol{u}^{\text{T}})/2,\tag{9}$$

where $\boldsymbol{S}$ is the strain rate tensor, $\boldsymbol{W}$ is the rotation rate tensor, $\nabla\boldsymbol{u}$ is the velocity divergence, and A_0 and A_{s} are coefficients. It can be seen that the coefficient of turbulent viscosity is the term which considers the mean strain and rotation rates, the angular velocity of the system rotation, and the turbulence fields.

The volume of fraction (VOF) method is used for capturing the free surface, which is accomplished by tracing the volume fraction of control volumes in the solution of the continuity equation. The fluid is usually divided into several phases, each of which can be written as

$$\frac{\partial\alpha_q}{\partial t}+\nabla\cdot\left(\alpha_q u_i\right)=0,\tag{10}$$

where α_q is the qth phase, and all phases are based on the following constraint:

$$\sum_{q=1}^{n}\alpha_q = 1, \tag{11}$$

where n is the quantity of phases.

The physical property of each phase is calculated by its volume fraction as in the following function:

$$\rho = \sum_{q=1}^{n}\rho_q\alpha_q, \tag{12}$$

$$\mu = \sum_{q=1}^{n}\mu_q\alpha_q. \tag{13}$$

3 Experimental setup

3.1 Experimental device

An independent type C LNG tank of 1000 m^3, which is designed to be installed at a LNG fuel bunker vessel, is investigated here. A model tank is used in this physical experiment at a scale of 1/17.8. The total length (L_{tt}) and outer diameter (D_o) of the test model tank are 1.910 m and 0.400 m, respectively (Fig. 2). The test model tank consists of a main tank and two heads (Model EHB 390×10PMMA JB/T 4746 (SETC, 2002)) (Fig. 2) with a thickness of 10 mm in the model. The main tank and heads are made from plexiglas pipeline and polyvinyl chloride (PVC), respectively. In the head and the top of the test model tank, seven holes for measuring sloshing pressure are set. The arrangement of monitor points is described in Fig. 3. The experimental fluid used in the experiment is water, its density and viscosity are 997.561 kg/m^3 and 8.887×10^{-4} Pa·s, respectively. About 5 ml red water-solubility dye is added to help in distinguishing the free surface. This dyeing method has been used in many studies (Souto-Iglesias et al., 2011; Jiang et al., 2014) and has little influence on the properties of the water.

The motion platform and its controller cabinet (Figs. 4a and 4b), which can simulate a ship motion with six degrees of freedom (DOFs), are applied to provide a sloshing motion. The parameters of the motion platform are listed in Table 1. Flush-mounted pressure sensors (Delorme et al., 2009) are used to capture loads induced by sloshing. The measuring ranges are 0–10 kPa, with an accuracy of 0.2% FS (full scale). In addition, with the application of a high-speed camera, the shape of the free surface can be traced at 50 pictures a second.

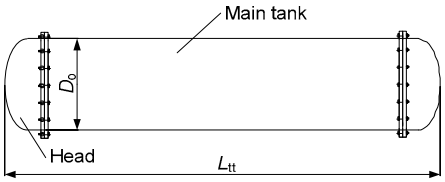

Fig. 2 Test model tank

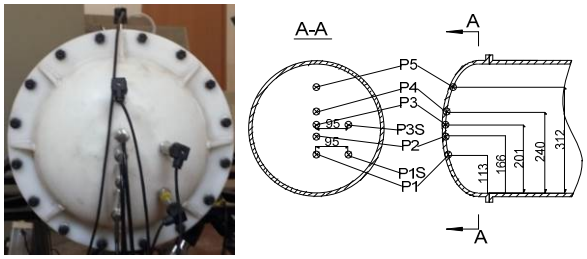

Fig. 3 Arrangement of monitor points for pressure senor (unit: mm)

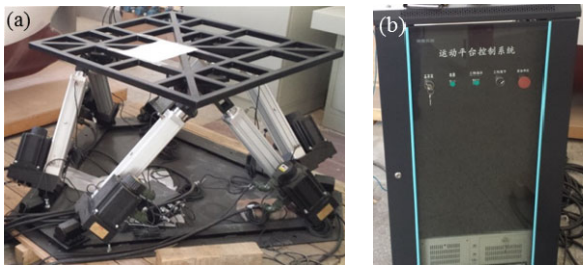

Fig. 4 Pictures of test rig used in this experiment
(a) 6-DOF motion platform; (b) Controller cabinet

Table 1 Parameters of 6-DOF motion platform

DOF	Max displacement	Velocity relative to central point
Surge	±240 mm	
Sway	±210 mm	±300 mm/s
Heave	±160 mm	
Pitch	±25°	
Roll	±25°	±50 °/s
Yaw	±35°	

3.2 Test case

As the length-diameter ratio of the test model tank is almost 1/5, the tank is very sensitive to longitudinal excitation. For a ship, roll, pitch, and heave are the most common situations (Wang et al.,

1998). Hence, pitch was selected to excite the test model tank. In this study, the filling level is measured by the inner diameter (D_i) of the model tank. Four test cases are chosen to verify the numerical method. The parameters of test cases are listed in Table 2, in which f_n represents the natural frequency.

Table 2 Parameters of test cases

Case	Filling level	Excitation frequency	Excitation amplitude (rad)
No. 1	$0.60D_i$	$1.0f_n$ (0.36 Hz)	0.052
No. 2	$0.60D_i$	$1.2f_n$ (0.40 Hz)	0.052
No. 3	$0.60D_i$	$1.0f_n$ (0.36 Hz)	0.087
No. 4	$0.25D_i$	$1.0f_n$ (0.22 Hz)	0.052

Free oscillation of a liquid is adopted to obtain the natural frequency at a specified filling level. To this end, the pressure time history is achieved after the tank is stopped at considerable velocity. Then, a fast Fourier transform is used to analyze the frequency domain of the pressure time history. The spectral peak frequency corresponding to the maximum pressure spectrum is the lowest order natural frequency. Considering the properties of the motion platform, the value of natural frequency can be derived to two decimal places, namely, 0.01 Hz.

To eliminate the effect of the initial situation, the pitch motion will be written as

$$\theta_m(t)=\begin{cases}\dfrac{\theta_A t}{20}\sin(2\pi ft), & 0\ \text{s}\le t\le 20\ \text{s},\\ \theta_A\sin(2\pi ft), & t>20\ \text{s},\end{cases} \tag{14}$$

where $\theta_m(t)$ is the radian or displacement of the model tank movement, θ_A is the maximum amplitude of excitation, f is the excitation frequency, and t is the time of excitation. It can be seen that the test model tank will take 20 s to get to the maximum amplitude.

4 Verification of the numerical simulation

4.1 Model configuration of tank without baffle ring

The inner surface of the test model tank is selected as the model for simulation. A Cartesian grid is used to mesh this model. Fig. 5 shows the internal grid of the model tank. The refinement process is applied to the boundary of model with a prism layer. The quantity of grids is about 435 000. On the basis that the Courant-Friedrichs-Lewy (CFL) number is less than 1, the time step is selected to be 0.002 s. The boundary condition of the vertical section is set to be symmetrical. The surfaces of model tank are set as a no-slip wall. The rigid motion of mesh vertices in entire fluid region is utilized to handle the tank's external excitation. In the present study, the motion is specified by a user-defined function and it is assumed that the moving component does not deform during motion.

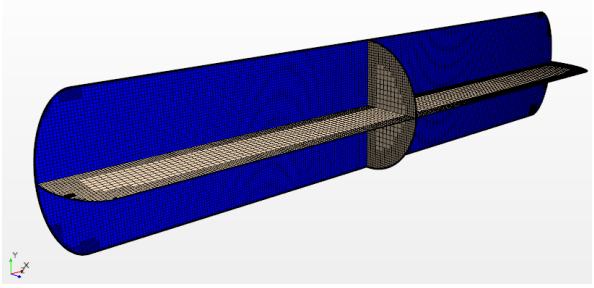

Fig. 5 Grid of the model tank

A 3D implicit unsteady solver is used to solve the viscosity flow in a tank by the collocated grid arrangement. The air is considered to be compressible, while the water is of constant density. The first order scheme is used for temporal discretization. The physical time of simulation is 15 oscillation periods after the excitation amplitude reaches the specified angle. The commercial CFD solver, STAR-CCM+ is adopted for all the simulations. Simulations are accomplished in an Intel (R) Xeon(R) CPU E5-2630 v4 @2.20 GHz (double CPU) workstation with 32.0 GB of RAM.

4.2 Verification

Based on the results of the experiments, the numerical simulation is verified qualitatively by the deformation of the free surface and compared quantitatively with the pressure time history of sloshing. The verification condition is the same as the test cases, under which severe sloshing will happen. However, in the test cases in this study, the pressure time histories are different between the $0.60D_i$ filling

level and others. There are double peaks in time pressure history under $0.60D_i$ filling level in case No. 1 (Fig. 6a). According to the relation between sloshing pressure and oscillation angle, it can be found that, when the oscillation frequency is close to the natural frequency, the impact pressure due to the violent motion of the free surface will be dominant and the first peak will be formed. Then, when the tank moves to the horizontal position, the liquid will push the tank head due to inertial force and gravity. Thus, it will produce the other peak. This opinion can be proved by Zhao and Chen (2015). Under $0.25D_i$ filling level, the single peak will appear after the tank reaches the maximum angle and moves to the horizontal position (Fig. 6b). The reason is that the smaller mass of liquid cannot produce the second impact on the head, although the excitation frequency is close to the natural one.

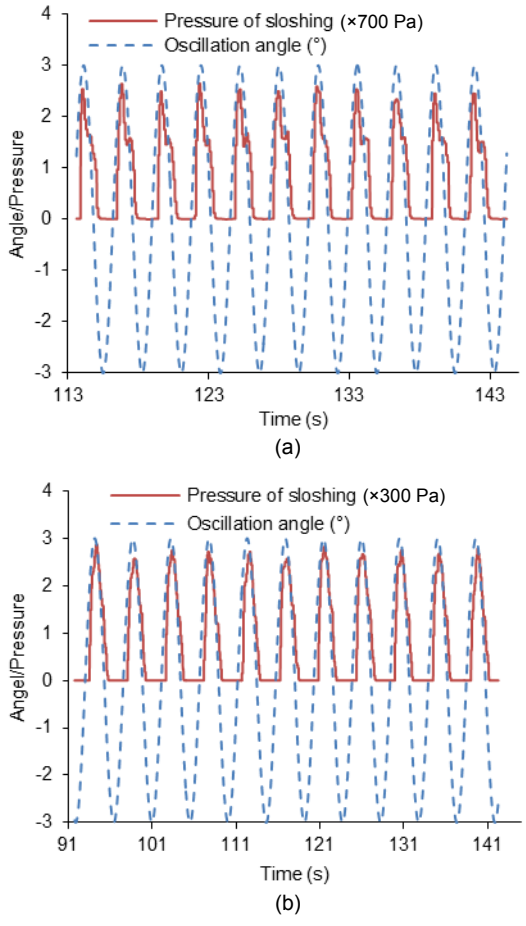

Fig. 6 Relation between sloshing pressure and oscillation angle
(a) Case No. 1 (monitor point P4); (b) Case No. 4 (monitor point P1)

The monitoring points P1, P2, P3S, and P4 are selected for validating the different cases. Comparisons of pressure time history between experiments and numerical simulations are shown in Figs. 7–10. In addition, the mean values of sloshing pressure after full excitation amplitude are compared between experiments and numerical simulations (Table 3). It can be seen that comparisons at all monitoring points show good agreement in the cases validated. The pressure of the monitoring point which is located at the free surface is strongly affected by deformation of that surface. Thus, there will be some deviations in numerical simulation under the resonance of sloshing in cases No. 1 and No. 2. However, it can be shown from the quantitative comparisons that the numerical method can predict the sloshing pressure well, including monitoring points near the free surface.

The shapes of the free surface in sloshing are also compared. According to the movement mode of the motion platform, the test model tank will rotate anticlockwise from the initial position. For convenience of description, the position of the tank at one

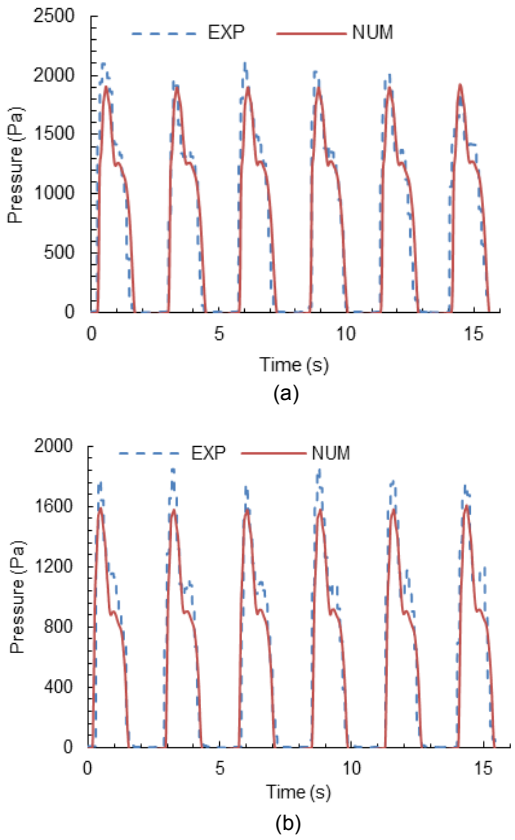

Fig. 7 Time histories of sloshing pressure (case No. 1)
(a) P3S; (b) P4. EXP: experimental; NUM: numerical

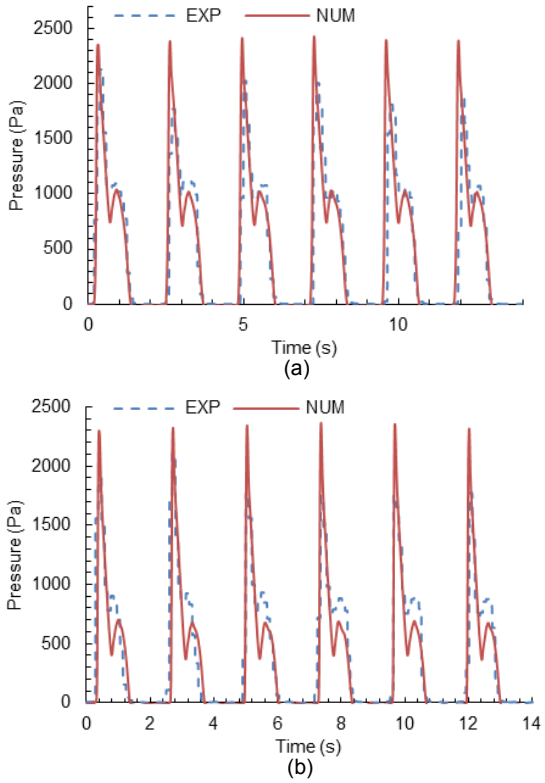

Fig. 8 Time histories of sloshing pressure (case No. 2)
(a) P3S; (b) P4

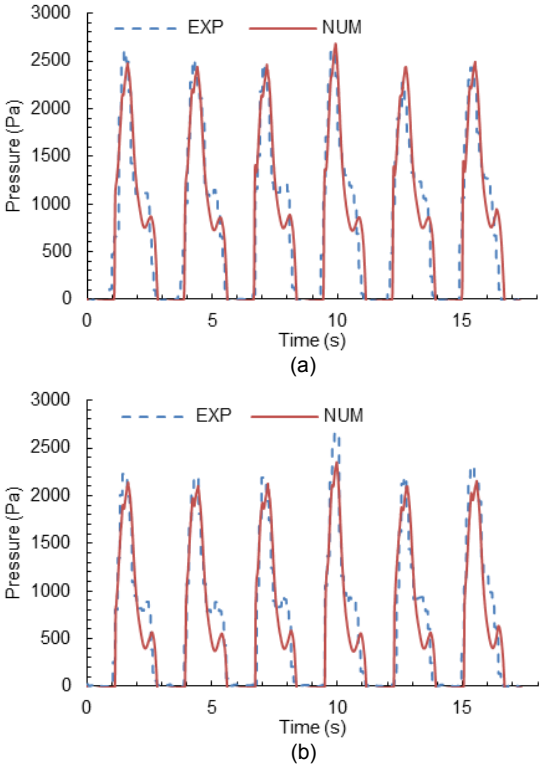

Fig. 9 Time histories of sloshing pressure (case No. 3)
(a) P3S; (b) P4

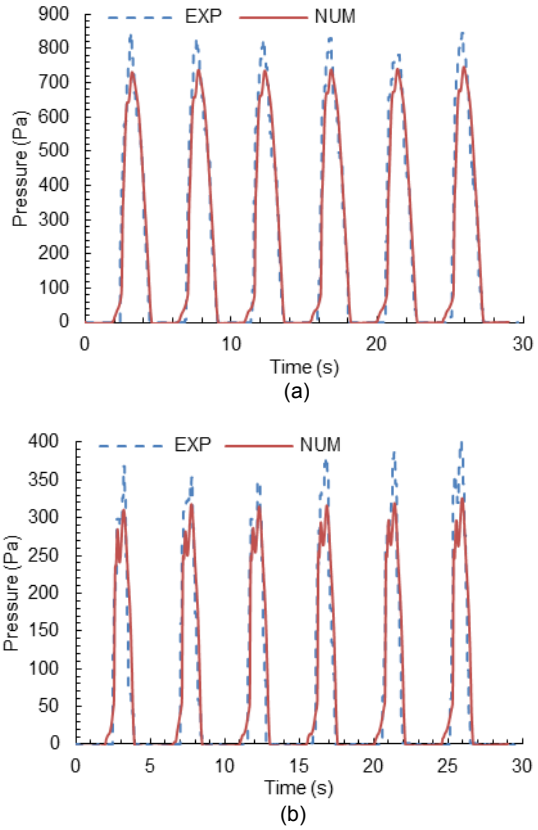

Fig. 10 Time histories of sloshing pressure (case No. 4)
(a) P1; (b) P2

Table 3 Comparison of results with different cases

Case	Monitor point	Mean sloshing pressure (Pa)		Error (%)
		Experimental	Numerical	
No. 1	P3S	639.07	622.50	−2.59
	P4	514.56	497.46	−3.32
No. 2	P3S	489.60	512.22	4.62
	P4	387.61	357.55	−7.75
No. 3	P3S	836.11	809.15	−3.23
	P4	682.61	624.31	−8.54
No. 4	P1	239.32	225.43	−5.80
	P2	69.77	70.68	1.30

designated period is selected as the basis of comparison of the free surface shapes. All the free surface profiles are captured when the maximum excitation angle is reached and compared at one period (T). As shown in Figs. 11a and 12a, the liquid travels as a bore from one side of tank to the other and there are a lot of air bubbles mixed in the free surface. Then, the liquid impacts the upper head of tank (Figs. 11b and 12b) and some free surface transforms into a jet flow

(Figs. 11c and 12c). When the oscillation angle increases, the deformation of the free surface becomes more violent and liquid impacts the top of the tank (Fig. 13). When the filling level arrives at $0.25D_i$, that is, shallow water (Faltinsen and Timokha, 2009), it can be seen that the flow of fluid is mild and transforms into a bore at the head of the test model tank, which is similar to the 3rd free-surface pattern (Bouscasse et al., 2013) (Fig. 14). Compared with the $0.60D_i$ filling level, the free surface will not strongly break but swirl like a bore after arriving at the head of the tank. In all, it was found that the numerical profile of the free surface generally coincided well with the experimental profile. This indicates that the VOF method is effective in capturing the shape of the free surface.

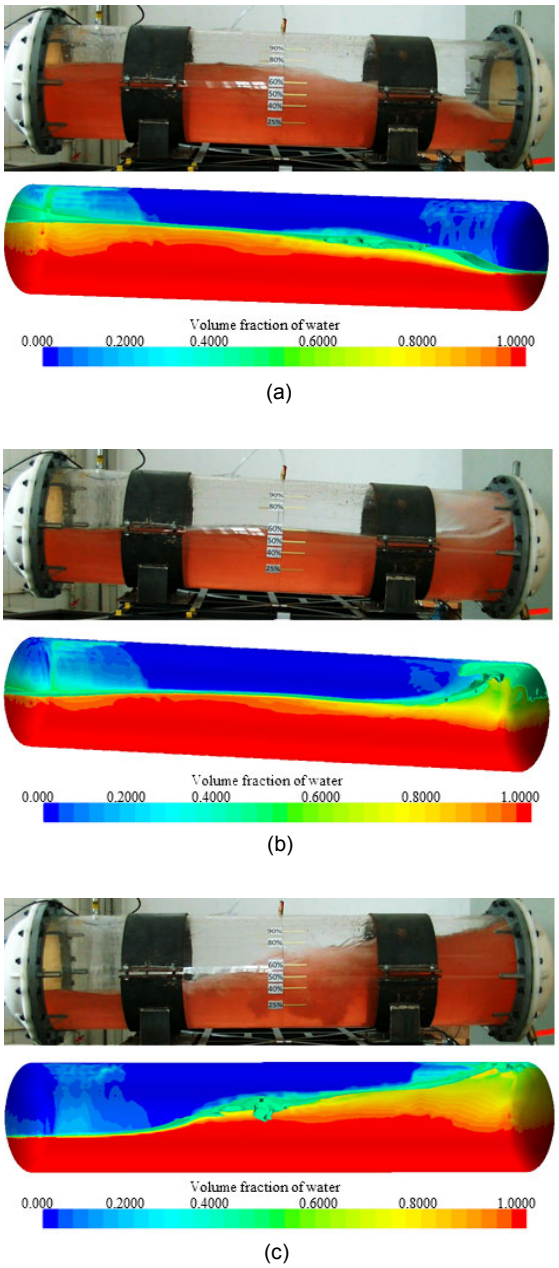

Fig. 11 Comparisons of computed and experimental free surface profiles of case No. 1
(a) 0.61*T*; (b) 0.94*T*; (c) 1.02*T*

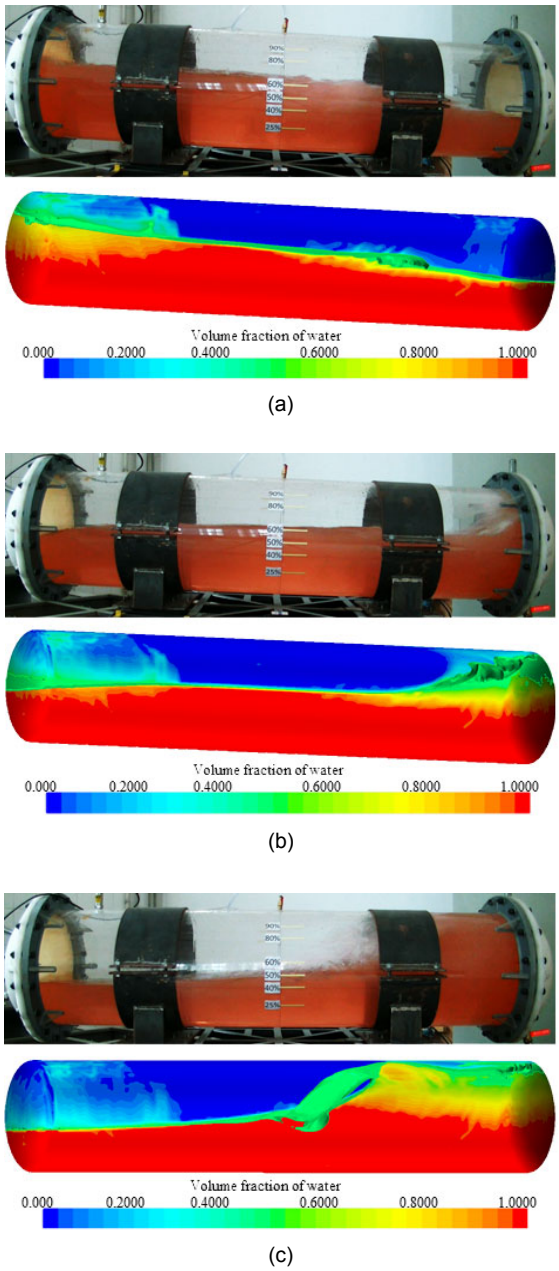

Fig. 12 Comparisons of computed and experimental free surface profiles of case No. 2
(a) 0.66*T*; (b) 0.87*T*; (c) 1.01*T*

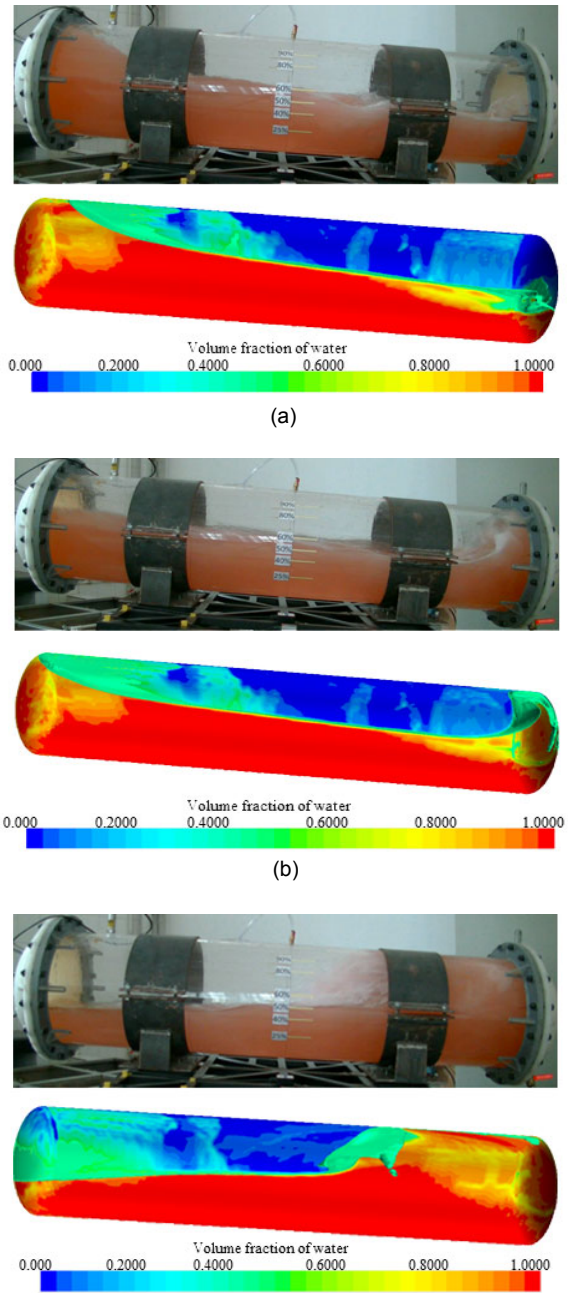

Fig. 13 Comparisons of computed and experimental free surface profiles of case No. 3
(a) 0.66T; (b) 0.70T; (c) 0.95T

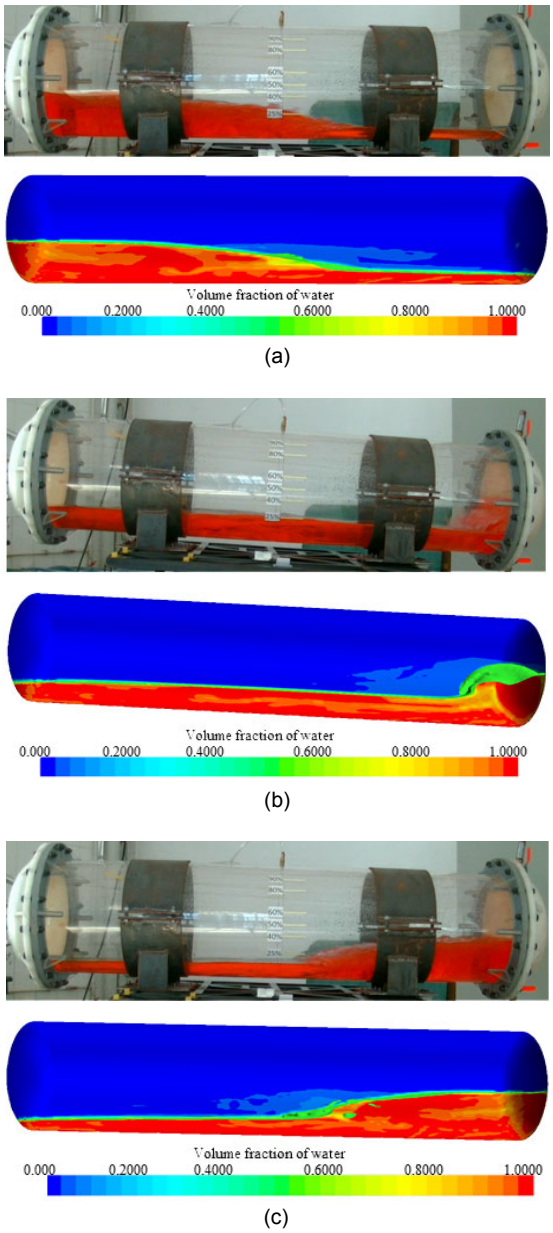

Fig. 14 Comparisons of computed and experimental free surface profiles of case No. 4
(a) 0.01T; (b) 0.52T; (c) 0.81T

5 Computational results and analysis

5.1 Model configuration of tank with baffle ring

The test model tank is selected to be the object of research. Two ring baffles are set in the tank. In the physical tests with the same experimental device, the sloshing characteristic at four filling levels (0.25D_i, 0.40D_i, 0.60D_i, and 0.80D_i) is investigated experimentally by wave patterns and sloshing pressures (Liu et al., 2017). Under different filling levels and oscillation frequencies, the sloshing pressures measured by monitor points near the free surface are compared with statistical values. These statistical values in each filling level are selected to be maximal under different excitation frequencies. It is found that the filling level of 0.60D_i brings the largest sloshing

pressure on the head of the model tank. Therefore, case No. 1 is selected to be the research condition. The parameters, which can describe the baffle ring, include the height (H), the position installation (P), the inclined angle (θ), and the thickness (t). The definition of these parameters is shown in Fig. 15. As the blockage effect of a vertical baffle is mainly used to decrease the horizontal velocity of liquid, ring baffles with inclined angles might also disturb the horizontal flow of fluid by forming vortices. Therefore, for the integrity of the study, the influence of that incline angle is considered. The ring baffles are installed about the midsection of the tank and the incline angles of the two ring baffles are equal. The parameters sensitivity on anti-sloshing is investigated by orthogonal test design and the numerical method, which has been verified above, is used to simulate sloshing under different parameters of the baffle ring.

Based on the validated numerical method above, the Cartesian grid is also employed for these simulations (Fig. 16). Considering their thickness and size, the refinement process is used on the surface of the ring baffles. Also, the prism layer is attached to the boundary of the model. The midsection of the model is specified as a symmetry condition and other components as a no-slip wall condition.

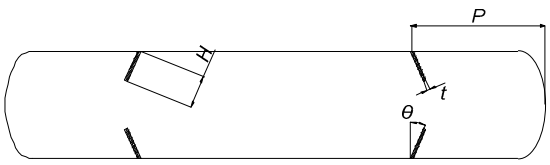

Fig. 15 Definition parameters of ring baffle

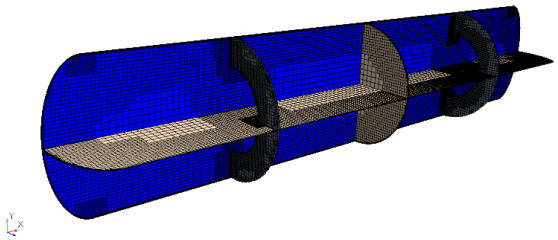

Fig. 16 Grid of tank with ring baffles

To verify the time and grid sensitivity of the solutions, the examination of grid dependence is first carried out. Three different grid systems, coarse, medium, and fine, are used to test the grid sensitivity of the solutions. The excitation condition is consistent with test case No. 1, and the simulation is carried out for duration of ten periods. The details of each grid and the results of relative error with a fine grid are shown in Table 4 and Fig. 17, from which it can be found that a coarse grid gives the worst result at monitoring point P4. Considering the pressure time histories, to capture the free surface movement accurately and efficiently, the medium grid system is chosen for the computations and three different time steps are considered: 0.004 s, 0.002 s, and 0.001 s. Table 5 gives the quantitative comparison of relative error with the time step 0.001 s. It can be seen from

Table 4 Details of grids and error of mean value with fine grid

Grid	Quantity	Error of mean value (%)	
		P1	P4
Coarse	370 194	1.80	−14.19
Baseline	446 692	4.22	2.05
Fine	618 519	–	–

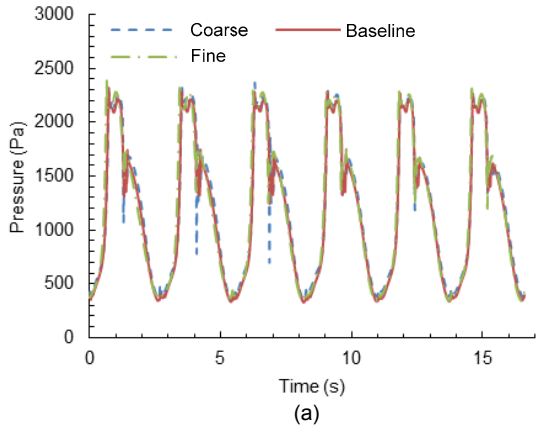

Fig. 17 Comparison of pressure time histories in monitoring points computed with different grids
(a) P1; (b) P4

Fig. 18 and Table 5 that results with the three kinds of time step show only small differences. However, the simulation used with 0.004 s will underestimate the peak of the sloshing pressure and so, for efficiency, a time step of 0.002 s is selected for the simulations.

Table 5 Error of mean value with time step of 0.001 s

Time step (s)	Error of mean value (%)	
	P1	P4
0.004	−0.38	−4.29
0.002	2.48	3.22

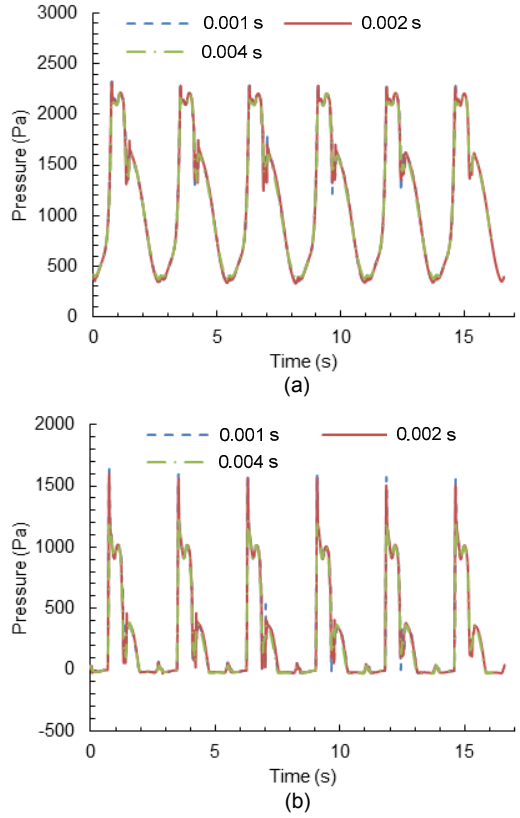

Fig. 18 Comparison of pressure time histories in monitoring points computed with different time steps
(a) P1; (b) P4

5.2 Design of orthogonal simulation experiment

The four definition parameters of the ring baffle are selected as factors in the orthogonal simulation experiment. All factors and their levels are listed in Table 6. The three levels of the height (H) of the ring baffle start from $0.10D_i$ with $0.10D_i$ steps and the absolute height in mm is given in Table 6 as well. From the point of view of a decrease in the length of free surface, the ring baffle is installed at $1/3L_{tt}$ and $2/3L_{tt}$. Then both ring baffles will be installed close to the head of the tank at the 1/4 and 1/5 length of the tank. The distance of ring baffles to the head of tank is also listed in Table 6. The maximum inclined angle is set to ±45° and the positive value is for the ring baffle rotating clockwise. Considering the size of grid, the thickness of the ring baffle is divided into three levels: 5 mm, 10 mm, and 15 mm. The interactions of all factors are neglected. As the factors and levels can not satisfy the standard orthogonal table, the commercial code IBM SPSS 19.0 is adopted to design the orthogonal simulation experiment (Table 7). For error analysis, a blank column of factor x, which has three levels, 1, 2, and 3, is added to the orthogonal table.

Table 6 Factors and levels in the orthogonal simulation experiment

Level	H	P	θ	t
1	$0.10D_i$ (38 mm)	630 mm (1/3)	0°	5 mm
2	$0.20D_i$ (76 mm)	472.5 mm (1/4)	−23°	10 mm
3	$0.30D_i$ (114 mm)	378 mm (1/5)	23°	15 mm
4			−45°	
5			45°	

5.3 Results and discussion

Through numerical simulation, the force time history on the head of the tank in the x direction is achieved after excitation at the maximum oscillation angle. The efficiency of the ring baffle is taken from the definition of Kim and Lee (2008) for reference. However, the horizontal force on the head of tank due to the sloshing pressure replaces the water height variation. Thus, the efficiency of the ring baffle is defined as

$$\eta_{\text{anti-sloshing}} = \frac{\sigma_{\text{unbaffled}} - \sigma_{\text{baffled}}}{\sigma_{\text{unbaffled}}}, \tag{15}$$

where σ is the square of deviation of force in x direction at the left head, and the subscript of σ specifies sloshing condition of tank with or without baffle ring.

The results of anti-sloshing are listed in Table 8. The mean values (K_i) of each level for the different factors and their ranges (R) are given (Table 9). By

Table 7 Orthogonal test design table

No.	Factor level				
	A (H)	B (θ)	C (t)	D (P)	E (x)
1	3	2	1	2	3
2	2	3	1	1	3
3	1	2	2	3	1
4	1	1	2	1	3
5	2	1	1	2	1
6	1	4	1	1	2
7	1	3	3	2	2
8	3	4	3	1	1
9	1	5	1	1	2
10	1	2	1	2	2
11	2	3	1	3	1
12	3	1	1	3	2
13	3	5	2	2	1
14	1	2	2	2	1
15	2	1	3	2	2
16	1	1	2	1	1
17	2	5	1	1	1
18	2	2	3	1	1
19	2	2	2	1	2
20	1	5	3	3	3
21	3	2	2	1	2
22	2	4	2	2	3
23	1	4	1	2	1
24	2	4	2	3	2
25	2	5	2	2	2

Table 8 Results of orthogonal simulation experiment

No.	$\eta_{\text{anti-sloshing}}$	No.	$\eta_{\text{anti-sloshing}}$	No.	$\eta_{\text{anti-sloshing}}$
1	0.07	10	0.09	18	0.40
2	0.31	11	0.62	19	0.17
3	0.16	12	0.55	20	0.33
4	0.15	13	0.37	21	0.68
5	0.15	14	0.55	22	0.63
6	0.13	15	0.50	23	0.65
7	0.16	16	0.58	24	0.60
8	0.31	17	0.59	25	0.78
9	0.04				

Table 9 Visual analysis of orthogonal simulation

Factor	K_1	K_2	K_3	K_4	K_5	R
A	1.1336	1.6435	1.8226	–	–	0.6890
B	1.6574	1.4743	1.5282	1.3570	1.3601	0.3004
C	1.4862	1.4904	1.4237	–	–	0.0667
D	1.6100	1.4662	1.2246	–	–	0.3854

comparison of the ranges, the order of effect of the four factors can be concluded as A>D>B>C. Based on the mean values of each level, it is found that the best scheme is $A_3B_1C_1D_1$. Moreover, the subject effect is analyzed by computation of variance (Table 10). In Table 10, d_f is the degree of factor; F is the ratio of S_f to S_σ; S_f is the quadratic sum of the average deviation of factors; S_σ is the quadratic sum of average deviation of error. The significance of factors A, B, and D is less than 0.05, so it could be concluded these factors have significant influence on the efficiency of anti-sloshing. Based on the value of F, the factor A, namely, the height of the ring baffle, can significantly reduce sloshing. The factor C, that is, the thickness of the baffle ring, hardly affects the efficiency of anti-sloshing. Also, it can be seen from the magnitude of the F value that the effect order is the same as the result in comparisons of range.

Table 10 Analysis of variance

Source	Type III sum of squares	d_f	Mean square	F	Significance
Corrected model	2.883	10	0.288	50.592	0.000
Intercept	41.227	1	41.227	7234.420	0.000
A	2.054	2	1.027	180.184	0.000
B	0.316	4	0.079	13.868	0.000
C	0.017	2	0.008	1.474	0.262
D	0.497	2	0.248	43.567	0.000
Error	0.080	14	0.006		
Total	57.382	25			
Corrected total	2.963	24			

Increasing the height of the ring baffle, i.e. the main factor, is the most effective method of sloshing reduction. However, increasing the size of the ring baffle can bring fatigue and transform the baffle into a sacrificial structure (Sanapala et al., 2016). Therefore, simulation tests are designed to indicate the most effective height for sloshing reduction. Test cases No. 1 and No. 3 (Table 2) are selected as the conditions of simulation, which means two different excitation angles will be used while other conditions are the same. The parameters of ring baffles are given in Table 11, in which No. 1 ring baffle is included in orthogonal simulation experiments (i.e. No. 4 in Table 7). No. 4 ring baffles are verified as the best

option in all the orthogonal simulation experiments. Likewise, Eq. (15) is selected as the criterion to evaluate the effectiveness of different ring baffles. As shown in Fig. 19, if the height of ring baffles is increased, the efficiency of suppressing sloshing will be improved. However, the rate of improvement in reducing sloshing slows considerably after the height of the ring baffles exceeds $0.20D_i$.

The mechanism of suppressing sloshing by means of ring baffles is also investigated numerically. The case No. 19 in the orthogonal table and the 2nd case in discussion of the height of the ring baffle are selected to compare the difference in anti-sloshing power of two types of ring baffle. Assuming that the thickness of the ring baffle is not the main effect factor, the case No. 2 in the orthogonal table is also used to discuss the effectiveness of the direction of inclined angle. At the same time ($0.275T$), there will be an elevation difference of the free surface between the middle and side of the tank when the fluid is about to impact the head (Figs. 20a, 21a, and 22a), because of the blockage effect of the ring baffles. If ring baffles with negative inclined angles are used, the transition of elevation near the ring baffles will be smooth (Fig. 21b). Both inclined baffles can reverse the direction of some fluid flow and can produce more vortices both in front and back of the ring baffle (Figs. 21c and 22c). As for the position of the baffle, cases No. 2 and No. 11 in the orthogonal table are used as comparators, and their motion of the free surface at different times in one period is shown. It is indicated that too large a distance between two ring baffles cannot suppress the velocity of the fluid in time and weakens the effectiveness of anti-sloshing. As the length of free surface in the middle part of tank increases, the elevation difference of free surface between the two ring baffles will rise (Figs. 23a and 23c) (p.772) and the free surface will break up after the fluid flows back (Fig. 23b).

Table 11 Parameters of ring baffles for analysis

No.	H	θ (°)	t (mm)	P (mm)
1	$0.10D_i$	0	10	630
2	$0.20D_i$			
3	$0.25D_i$			
4	$0.30D_i$			

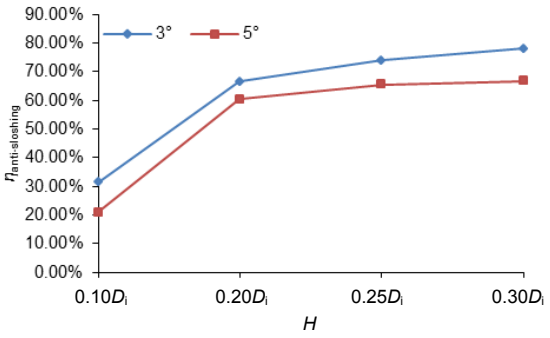

Fig. 19 Efficiency of different heights of ring baffles with different excitation angles

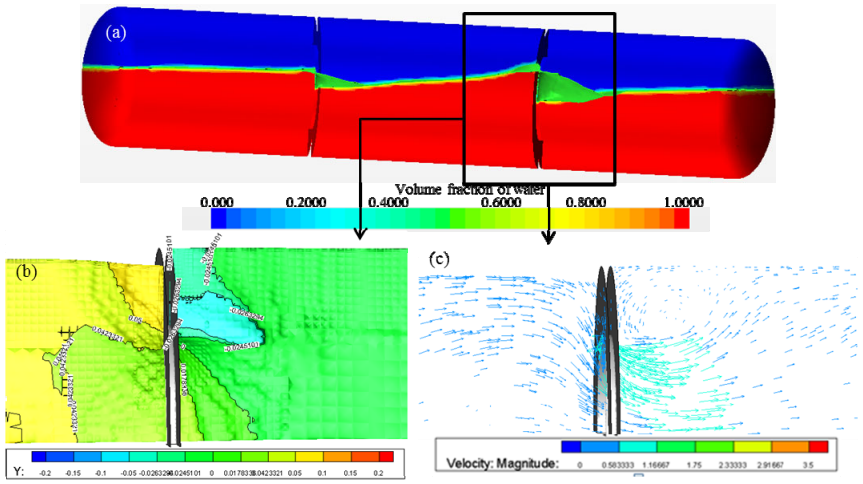

Fig. 20 Flow of fluid near a vertical ring baffle
(a) Volume of fraction in front view; (b) Elevation of free surface in top view; (c) Velocity vector of fluid in top view

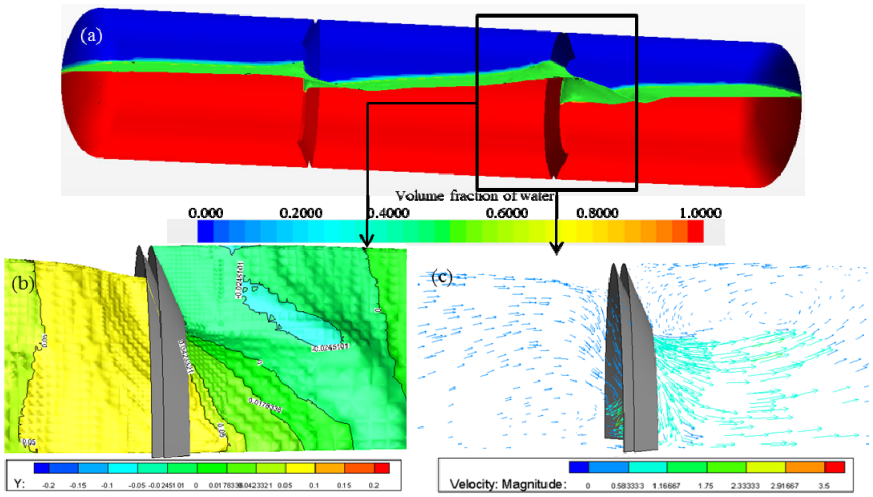

Fig. 21 Flow of fluid near ring baffle with negative inclined angle
(a) Volume of fraction in front view; (b) Elevation of free surface in top view; (c) Velocity vector of fluid in top view

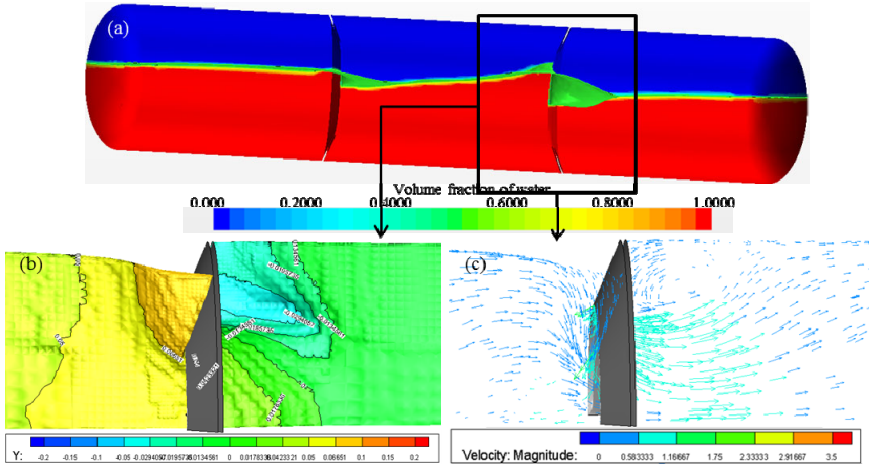

Fig. 22 Flow of fluid near ring baffle with positive inclined angle
(a) Volume of fraction in front view; (b) Elevation of free surface in top view; (c) Velocity vector of fluid in top view

6 Conclusions

In this study, the characteristics of a ring baffle in suppressing sloshing are investigated by a numerical method, which is validated through physical experiments. The pressure time history of monitoring points in a physical experiment and the shape of the free surface are selected as the criterion for quantitative validation. In addition, the phenomenon of physical experiments under different experimental conditions is discussed. An orthogonal test design is used to analyze the sensitivity of four definition parameters of a ring baffle, and the cases in an orthogonal table are computed by a validated numerical method. Also, the factors of ring baffle with the greatest influence in reducing sloshing are determined by analysis of variance and those most significant factors and the mechanisms of anti-sloshing with a ring baffle are discussed.

It can be concluded that:

1. The height, the installed position, and the installed angle can have great influence on suppressing sloshing. The thickness of the baffle has little effect.

2. The height of the ring baffle is proportional to its efficiency in anti-sloshing through analysis of orthogonal simulation experiments. However, the room for improvement in suppressing sloshing

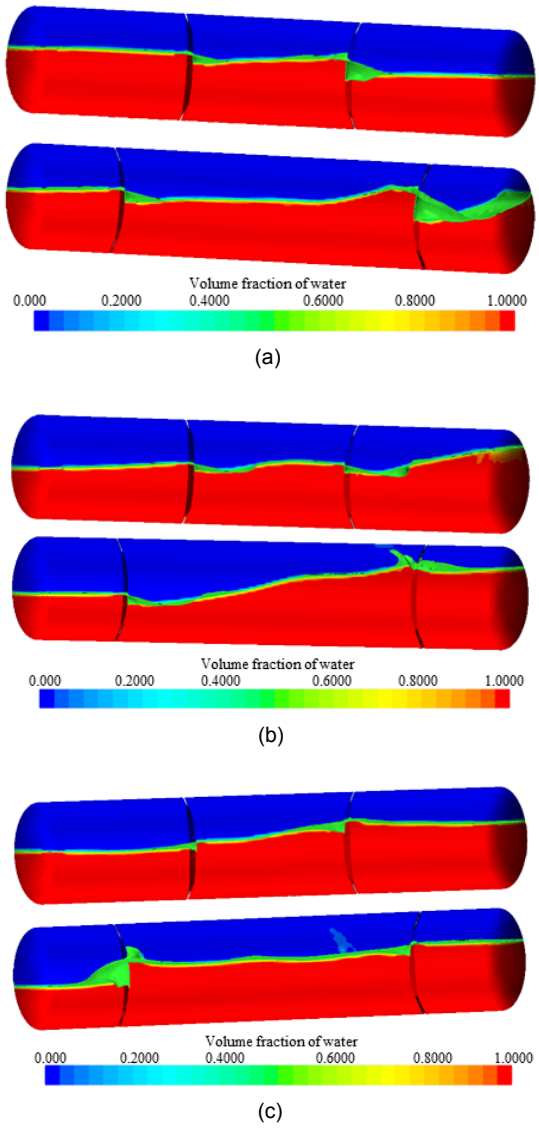

Fig. 23 Deformation of free surface during: (a) 0.745*T*; (b) 0.932*T*; (c) 1.148*T*

decreases after the height of the baffle exceeds $0.20D_i$.

3. A vertical ring baffle is more effective than an inclined baffle in restraining the velocity of the fluid as it provides a greater blockage effect. There is also a difference for different directions of the incline of the baffle. When the ring baffle is inclined, it is more effective in reducing sloshing when the top of ring baffle rotates away from the head of the tank. However, this difference of sloshing reduction decreases as the inclined angle is increased.

4. The efficiency of anti-sloshing declines when the ring baffle is set close to the ends of tank, as there is an increased length of free surface and elevation difference of the free surface in the middle of tank.

5. According to the analysis results obtained for an independent type C LNG tank with a longitudinal excitation, a ring baffle performs well in suppressing sloshing when suitably designed in height, position, and inclined angle.

Reference

Akyıldız H, Erdem Ünal N, Aksoy H, 2013. An experimental investigation of the effects of the ring baffles on liquid sloshing in a rigid cylindrical tank. *Ocean Engineering*, 59:190-197. https://doi.org/10.1016/j.oceaneng.2012.12.018

Bouscasse B, Antuono M, Colagrossi A, et al., 2013. Numerical and experimental investigation of nonlinear shallow water sloshing. *International Journal of Nonlinear Sciences and Numerical Simulation*, 14(2):123-138. https://doi.org/10.1515/ijnsns-2012-0100

Celebi MS, Akyildiz H, 2002. Nonlinear modeling of liquid sloshing in a moving rectangular tank. *Ocean Engineering*, 29(12):1527-1553. https://doi.org/10.1016/S0029-8018(01)00085-3

Cho IH, Kim MH, 2016. Effect of dual vertical porous baffles on sloshing reduction in a swaying rectangular tank. *Ocean Engineering*, 126:364-373. https://doi.org/10.1016/j.oceaneng.2016.09.004

Delorme L, Colagrossi A, Souto-Iglesias A, et al., 2009. A set of canonical problems in sloshing, Part I: pressure field in forced roll-comparison between experimental results and SPH. *Ocean Engineering*, 36(2):168-178. https://doi.org/10.1016/j.oceaneng.2008.09.014

Faltinsen OM, Timokha AN, 2009. Sloshing. Cambridge University Press, Cambridge, UK.

Jiang MR, Ren B, Wang GY, et al., 2014. Laboratory investigation of the hydroelastic effect on liquid sloshing in rectangular tanks. *Journal of Hydrodynamics*, *Ser. B*, 26(5):751-761. https://doi.org/10.1016/S1001-6058(14)60084-6

Kang N, Liu K, 2010. Influence of baffle position on liquid sloshing during braking and turning of a tank truck. *Journal of Zhejiang University-SCIENCE A* (*Applied Physics & Engineering*), 11(5):317-324. https://doi.org/10.1631/jzus.A0900521

Kim HS, Lee YS, 2008. Optimization design technique for reduction of sloshing by evolutionary methods. *Journal of Mechanical Science and Technology*, 22(1):25-33. https://doi.org/10.1007/s12206-007-1003-z

Liu G, Lin Y, Guan G, et al., 2017. Experimental study of sloshing pattern on LNG independent C type tank. *Journal of Dalian University of Technology*, 57(5):467-475 (in Chinese). https://doi.org/10.7511/dllgxb201705005

Lloyd N, Vaiciurgis E, Langrish TAG, 2002. The effect of

baffle design on longitudinal liquid movement in road tankers: an experimental investigation. *Process Safety and Environmental Protection*, 80(4):181-185. https://doi.org/10.1205/095758202320439137

Lu Y, Hu AK, Liu YC, et al., 2016. A meshless method based on moving least squares for the simulation of free surface flows. *Journal of Zhejiang University-SCIENCE A* (*Applied Physics & Engineering*), 17(2):130-143. https://doi.org/10.1631/jzus.A1500053

Panigrahy PK, Saha UK, Maity D, 2009. Experimental studies on sloshing behavior due to horizontal movement of liquids in baffled tanks. *Ocean Engineering*, 36(3-4):213-222. https://doi.org/10.1016/j.oceaneng.2008.11.002

Sanapala VS, Velusamy K, Patnaik BSV, 2016. CFD simulations on the dynamics of liquid sloshing and its control in a storage tank for spent fuel applications. *Annals of Nuclear Energy*, 94:494-509. https://doi.org/10.1016/j.anucene.2016.04.018

SETC (State Economic and Trade Commission), 2002. Formed Heads for Steel Pressure Vessels, JB/T 4746-2002. National Standard of the People's Republic of China (in Chinese).

Souto-Iglesias A, Botia-Vera E, Martín A, et al., 2011. A set of canonical problems in sloshing. Part 0: experimental setup and data processing. *Ocean Engineering*, 38(16):1823-1830. https://doi.org/10.1016/j.oceaneng.2011.09.008

Wang DY, Jin XD, Li LY, 1998. On model experiment of sloshing in tanks. *Journal of Shanghai Jiaotong University*, 32(11):114-117 (in Chinese). https://doi.org/10.16183/j.cnki.jsjtu.1998.11.025

Wei ZJ, Faltinsen OM, Lugni C, et al., 2015. Sloshing-induced slamming in screen-equipped rectangular tanks in shallow-water conditions. *Physics of Fluids*, 27(3):032104. https://doi.org/10.1063/1.4913983

Wemmenhove R, Loots E, Luppes R, et al., 2005. Modeling two-phase flow with offshore applications. International Conference on Offshore Mechanics and Arctic Engineering, p.993-1001. https://doi.org/10.1115/OMAE2005-67460

Xue MA, Lin PZ, Zheng JH, et al., 2013. Effects of perforated baffle on reducing sloshing in rectangular tank: experimental and numerical study. *China Ocean Engineering*, 27(5):615-628. https://doi.org/10.1007/s13344-013-0052-6

Yu YM, Ma N, Fan SM, et al., 2017. Experimental and numerical studies on sloshing in a membrane-type LNG tank with two floating plates. *Ocean Engineering*, 129:217-227. https://doi.org/10.1016/j.oceaneng.2016.11.029

Zhang JW, Wu WQ, Hu JQ, 2016. A numerical study of the effects of the longitudinal baffle on nickel ore slurry sloshing in a prismatic cargo hold. *Marine Structures*, 46:149-166. https://doi.org/10.1016/j.marstruc.2016.01.003

Zhao YC, Chen HC, 2015. Numerical simulation of 3D sloshing flow in partially filled LNG tank using a coupled level-set and volume-of-fluid method. *Ocean Engineering*, 104:10-30. https://doi.org/10.1016/j.oceaneng.2015.04.083

中文概要

题　目： **LNG 独立 C 型罐制荡环的制荡效应数值研究**

目　的： 制荡挡板由于其安装方便并可以大幅减弱液舱半载时的晃荡效应而备受关注。本文基于试验验证的计算流体动力学方法，对环型挡板的制荡效应影响因素进行分析，以确定环形挡板中影响制荡效率的主要参数。

创新点： 1. 通过正交设计与数值模拟的结合，得到影响环形挡板制荡效率的主要因素。2. 结合正交试验的分析结果及环形挡板制荡机理数值分析，得出改进环形挡板制荡效率的方案。

方　法： 1. 通过物理试验对数值模拟方法进行验证；2. 通过正交试验设计，制定环形挡板参数的数值试验表（表 7），并根据计算结果，对参数的制荡效率影响进行分析（表 8 和 9）；3. 对主影响参数进行重点分析，得出其制荡效率的变化规律（图 19）；4. 对环形挡板的制荡机理进行分析，并对正交试验结果中各参数水平的影响进行验证。

结　论： 1. 环形挡板的高度、倾斜角度以及安装位置均对其制荡效率有显著影响，而环形挡板的厚度影响较小。2. 环形挡板的 4 个参数中，高度因素的影响效果最显著，但是，当高度增至罐体直径的 20%时，制荡效率提升速度变得不明显。3. 相比于倾斜挡板会产生较多涡流耗散，当环形挡板处于竖直状态时，其较强的阻隔效应可以提供更多的制荡效果；挡板倾斜的方向对制荡效果有一定的影响，但该影响会随着倾斜角度的增大而减小。4. 增大两个环形挡板的间距，将增加自由液面的长度，并延缓挡板约束流速的效率，从而减弱挡板的制荡效果。

关键词： 晃荡；环形挡板；LNG独立C型罐；敏感性分析